Mon. Not. R. Astron. Soc. **000**, 000–000 (0000) Printed 11 November 2007 (MN LaTeX style file v2.2)

Chandra spectroscopy of the hot star β Crucis and the discovery of a pre-main-sequence companion

David H. Cohen,[1⋆] Michael A. Kuhn,[1†] Eric L. N. Jensen,[1] Marc Gagné,[2] Nathan A. Miller[3]

[1] *Swarthmore College Department of Physics and Astronomy, Swarthmore, Pennsylvania 19081*
[2] *West Chester University of Pennsylvania, Department of Geology and Astronomy, West Chester, Pennsylvania 19383*
[3] *University of Wisconsin-Eau Claire, Department of Physics and Astronomy, Eau Claire, Wisconsin 54702*

11 November 2007

ABSTRACT

In order to test the O star wind-shock scenario for X-ray production in less luminous stars with weaker winds, we made a pointed 74 ks observation of the nearby early B giant, β Cru (B0.5 III), with the *Chandra* High Energy Transmission Grating Spectrometer. We find that the X-ray spectrum is quite soft, with a dominant thermal component near 3 million K, and that the emission lines are resolved but quite narrow, with half-widths of 150 km s^{-1}. The forbidden-to-intercombination line ratios of Ne IX and Mg XI indicate that the hot plasma is distributed in the wind, rather than confined right at the photosphere. It is difficult to understand the X-ray data in the context of the standard wind-shock paradigm for OB stars, primarily because of the narrow lines, but also because of the high X-ray production efficiency. A scenario in which the bulk of the outer wind is shock heated is broadly consistent with the data, but not very well motivated theoretically. It is possible that magnetic channeling could explain the X-ray properties, although no field has been detected on β Cru. We detected periodic variability in the hard ($h\nu > 1$ keV) X-rays, modulated on the known optical period of 4.58 hours, which is the period of the primary β Cephei pulsation mode for this star. We also have detected, for the first time, an apparent companion to β Cru at a projected separation of $4''$. This companion was likely never seen in optical images because of the presumed very high contrast between it and β Cru in the optical. However, the brightness contrast in the X-ray is only 3:1, which is consistent with the companion being an X-ray active low-mass pre-main-sequence star. The companion's X-ray spectrum is relatively hard and variable, as would be expected from a post T Tauri star. The age of the β Cru system (between 8 and 11 Myr) is consistent with this interpretation which, if correct, would add β Cru to the roster of Lindroos binaries – B stars with low-mass pre-main-sequence companions.

Key words: stars: early-type – stars: mass-loss – stars: oscillations – stars: pre-main-sequence – stars: winds, outflows – stars: individual: β Cru – X-rays: stars

1 INTRODUCTION

X-ray emission in normal O and early B stars is generally thought to arise in shocked regions of hot plasma embedded in the fast, radiation-driven stellar winds of these very luminous objects. High-resolution X-ray spectroscopy of a handful of bright O stars has basically confirmed this scenario (Kahn et al. 2001; Kramer et al. 2003; Cohen et al. 2006; Leutenegger et al. 2006). The key diagnostics are line profiles, which are Doppler broadened by the wind outflow, and the forbidden-to-intercombination (f/i) line ratios in helium-like ions of Mg, Si, and S, which are sensitive to the distance of the shocked wind plasma from the photosphere. Additionally, these O stars typically show rather soft spectra and little X-ray variability, both of which are consistent with the theoretical predictions of the line-driven instability (LDI) scenario (Owocki et al. 1988) and in contrast to observations of magnetically active coronal sources and magnetically channeled wind sources.

In order to investigate the applicability of the LDI wind-

⋆ E-mail: cohen@astro.swarthmore.edu
† Current address: Department of Astronomy and Astrophysics, Penn State University, University Park, Pennsylvania 16802

shock scenario to early B stars, we have obtained a pointed *Chandra* grating observation of a normal early B star, β Crucis (B0.5 III). The star has a radiation-driven wind but one that is much weaker than those of the O stars that have been observed with *Chandra* and *XMM-Newton*. Its mass-loss rate is at least two and more likely three orders of magnitude lower than that of the O supergiant ζ Pup, for example. Our goal is to explore how wind-shock X-ray emission changes as one looks to stars with weaker winds, in hopes of shedding more light on the wind-shock mechanism itself and also on the properties of early B star winds in general. We will apply the same diagnostics that have been used to analyze the X-ray spectra of O stars: line widths and profiles, f/i ratios, temperature analysis from global spectral modeling, and time-variability analysis.

There are two other properties of this particular star that make this observation especially interesting: β Cru is a β Cephei variable, which will allow us to explore the potential connection among pulsation, winds, and X-ray emission; and there are several low-mass pre-main-sequence stars in the vicinity of β Cru. This second fact became potentially quite relevant when we unexpectedly discovered a previously unknown X-ray source four arc seconds from β Cru in the *Chandra* data.

In the next section, we discuss the properties of β Cru. In §3 we present the *Chandra* data. In §4 we analyze the spectral and time-variability properties of β Cru. In §5 we perform similar analyses of the newly discovered companion. We discuss the implications of the analyses of both β Cru and the companion as well as summarize our conclusions in §6.

2 THE β Cru SYSTEM

A member of the Lower Centaurus Crux (LCC) subgroup of the Sco-Cen OB association[1], β Cru is located at a distance of only 108 pc (Perryman et al. 1997). With a spectral type of B0.5, this makes β Cru – also known as Becrux, Mimosa, and HD 111123 – extremely bright. In fact, it is the 19th brightest star in the sky in the V band, and as a prominent member of the Southern Cross (Crux), it appears in the flags of five nations in the Southern Hemisphere, including Australia, New Zealand, and Brazil.

The fundamental properties of β Cru have been extensively studied and, in our opinion, quite well determined now, although binarity and pulsation issues make some of this rather tricky. In addition to the Hipparcos distance, there is an optical interferometric measurement of the star's angular diameter (Hanbury Brown et al. 1974), and thus a good determination of its radius. It is a spectroscopic binary (Heintz 1957) with a period of 5 years (Aerts et al. 1998). Careful analysis of the spectroscopic orbit in conjunction with the brightness contrast at 4430 Å from interferometric measurements (Popper 1968), and comparison to model atmospheres, enable determinations of the mass, effective temperature, and luminosity of β Cru (Aerts et al. 1998). The log g value and mass imply a radius that is consistent with that derived from the angular diameter and parallax distance, giving us additional confidence that the basic stellar parameters are now quite well constrained. The projected rotational velocity is low ($v \sin i = 35$ km s^{-1}), but the inclination is also low, between 15° and 20° (Aerts et al. 1998). This implies $v_{\rm rot} \approx 120$ km s^{-1} and combined with $R_* = 8.4$ R$_\odot$, the rotational period is $P_{\rm rot} \approx 3\overset{\rm d}{.}6$. These properties are summarized in Table 1.

With $T_{\rm eff} = 27,000 \pm 1000$ K, β Cru lies near the hot edge of the beta Cephei pulsation strip in the HR diagram (Stankov & Handler 2005). Three different non-radial pulsation modes with closely spaced periods between 4.03 and 4.59 hours have been identified spectroscopically (Aerts et al. 1998). Modest radial velocity variations are seen at the level of a few km s^{-1} overall, with some individual pulsation components having somewhat larger amplitudes (Aerts et al. 1998). The observed photometric variability is also modest, with amplitudes of a few hundredths of a magnitude seen only in the primary pulsation mode (Cuypers 1983). More recent, intensive photometric monitoring with the star tracker aboard the WIRE satellite has identified the three spectroscopic periods and found two additional very low amplitude (less than a millimagnitude), somewhat longer period components (Cuypers et al. 2002). The first three modes are identified with azimuthal wavenumbers $\ell = 1$, 3, and 4, respectively (Aerts et al. 1998; Cuypers et al. 2002).

The wind properties of β Cru are not very well known, as is often the case for non-supergiant B stars. The standard theory of line-driven winds (Castor, Abbott, & Klein 1975) (CAK) enables one to predict the mass-loss rate and terminal velocity of a wind given a line list and stellar properties. There has not been much recent work on applying CAK theory to B stars, as the problem is actually significantly harder than for O stars, because B star winds have many fewer constraints from data and the ionization/excitation conditions are more difficult to calculate accurately. With those caveats, however, we have used the CAK parameters from Abbott (1982) and calculated the mass-loss rate and terminal velocity using the stellar parameters in Table 1 and the formalism described by Kudritzki et al. (1989). The mass-loss rate is predicted to be about 10^{-8} M$_\odot$ yr^{-1} and the terminal velocity, $v_\infty \approx 2000$ km s^{-1}. There is some uncertainty based on the assumed ionization balance of helium, as well as the uncertainty in the stellar properties (gravity, effective temperature, luminosity), and whatever systematic errors exist in the line list. Interestingly, *IUE* observations show very weak wind signatures - in Si IV and C IV, with no wind signature at all seen in C III. The C IV doublet near 1550 Å has a blue edge velocity of only 420 km s^{-1}, while the blue edge velocity of the Si IV line is slightly smaller. The products of the mass-loss rate and the ionization fraction of the relevant ion are roughly 10^{-11} M$_\odot$ yr^{-1} for both of these species (Prinja 1989). Either the wind is much weaker than CAK theory (using Abbott's parameters) predicts or the wind has a very unusual ionization structure. We will come back to this point in §6.

[1] The star's proper motion has been taken to be discordant with the LCC by some authors, but these determinations have been affected by a spectroscopic binary companion, which has an orbital period of 5 years. The rate of orbital angular displacement of β Cru is similar to its proper motion.

Table 1. Properties of β Cru

MK Spectral Type	B0.5 III	Hiltner et al. (1969).
Distance (pc)	108 ± 7	Hipparcos (Perryman et al. 1997).
Age (Myr)	8 to 11	Lindroos (1985); de Geus et al. (1989).
$\theta_{\rm LD}$ (mas)	$0.722 \pm .023$	Hanbury Brown et al. (1974).
Mass ($M_\odot$)	16	Aerts et al. (1998).
$T_{\rm eff}$ (K)	$27,000 \pm 1000$	Aerts et al. (1998).
$\log g$	3.6 ± 0.1; 3.8 ± 0.1	Aerts et al. (1998); Mass from Aerts et al. (1998) combined with radius.
$v \sin i$ (km s^{-1})	35	(Uesugi & Fukuda 1982).
$L/L_\odot$	3.4×10^4	Aerts et al. (1998).
$R/R_\odot$	8.4 ± 0.6	From distance (Perryman et al. 1997) and $\theta_{\rm LD}$ (Hanbury Brown et al. 1974).
Pulsation periods (hr)	4.588, 4.028, 4.386, 6.805, 8.618	Aerts et al. (1998); Cuypers et al. (2002).
$\dot{M}$ (M$_\odot$ yr^{-1})	10^{-8}	Theoretical calculation, using Abbott (1982).
$\dot{M}q$ (M$_\odot$ yr^{-1})	10^{-11}	Product of mass-loss rate and ionization fraction of C IV (Prinja 1989).
v_∞ (km s^{-1})	2000	Theoretical calculation, using Abbott (1982).
v_∞ (km s^{-1})	420	Based on C IV absorption feature blue edge (Prinja 1989).

The LCC has an age of 11 Myr (de Geus et al. 1989), and β Cru has been claimed to have an evolutionary age of 8 Myr (Lindroos 1985), though the distance was much more uncertain when this work was done. Its true age probably can only be said to be roughly within this range. As such, β Cru has evolved off the main sequence, but not very far. Its spectroscopic binary companion is a B2 star that is still on the main sequence (Aerts et al. 1998). There are two other purported wide visual companions listed in the Washington Double Star catalog (Worley & Douglass 1997), with separations of 44″ and 370″, although they are almost certainly not physical companions of β Cru (Lindroos 1985).

A small group of X-ray bright pre-main-sequence (PMS) stars within about a degree of β Cru was discovered by *ROSAT* (Park & Finley 1996). These stars are likely part of the huge low-mass PMS population of the LCC (Feigelson & Lawson 1997). They have recently been studied in depth (Alcalá et al. 2002), and four of the six have been shown to be likely post-T-Tauri stars (and one of those is a triple system). They have H_α in emission, strong Li 6708 Å absorption, and proper motions consistent with LCC membership.

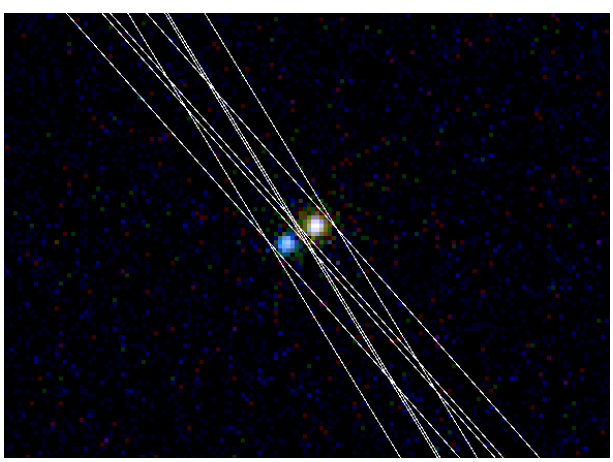

Figure 1. Image of the center of the ACIS detector, showing the zeroth order spectra of β Cru and its newly discovered companion. North is up and east is left. β Cru is the source to the northwest. Its position is coincident with the optical position of β Cru to within the positional accuracy of *Chandra*. The companion is to the southeast, at a separation of 4.0″ and with a position angle relative to β Cru of 120°. The extraction regions for the MEG and HEG (both positive and negative orders) are indicated for both sources. It can be seen in this image that the position angle is nearly perpendicular to the dispersion directions (for both the MEG and HEG) and thus that the dispersed spectra of the two sources can be separated. In the on-line color version of this figure, hard counts ($h\nu > 1$ keV) are blue, soft counts ($h\nu < 0.5$ keV) are red, and counts with intermediate energies are green. It can easily be seen in the color image that the X-ray emission of the companion is dramatically harder than β Cru.

3 THE *Chandra* DATA

We obtained the data we report on in this paper in a single long pointing on 28 May 2002, using the ACIS-S/HETGS configuration. We reran the pipeline reduction tasks in CIAO 3.3 using CALDB 3.2, and extracted the zeroth order spectrum and the dispersed first order MEG and HEG spectra of both β Cru and the newly discovered companion. The zeroth order spectrum of a source in the *Chandra* HETGS/ACIS-S is essentially an image created by source photons that pass directly through the transmission gratings without being diffracted. The ACIS CCD detectors themselves have some inherent energy discrimination so a low-resolution spectrum can be produced from these zeroth-order counts.

The zeroth order spectrum of each source has very little pileup ($\sim 1\%$), and the grating spectra have none. The HEG spectra and the higher order MEG spectra have almost no source counts, so all of the analysis of dispersed spectra we report on here involves just the MEG ± 1 order. We made observation-specific rmfs and garfs and performed our spectral analysis in both XSPEC 11.3.1 and ISIS 1.4.8. We performed time-variability analysis on both binned light curves and unbinned photon event tables using custom-written codes.

The observation revealed only a small handful of other possible sources in the field, which we identified using the CIAO task *celldetect* with the threshold parameter set to a value of 3. We extracted background-subtracted source counts from three weak sources identified with this procedure. Their signal-to-noise ratios are each only slightly above

Table 2. Point sources in the field

Name(s)	RA[a]	Dec.	total counts[b]	X-ray flux[c] (10^{-14} ergs s^{-1} cm^{-2})
β Cru A; Mimosa; Becrux; HD 111123	12 47 43.35	−59 41 19.2	3803 ± 12	186 ± 1
β Cru D; CXOU J124743.8-594121	12 47 43.80	−59 41 21.3	1228 ± 12	$57.3 \pm .6$
CXOU J124752.5-594345	12 47 52.53	−59 43 45.8	25.9 ± 8.6	$1.58 \pm .52$
CXOU J124823.9-593611	12 48 23.91	−59 36 11.8	47.4 ± 10.4	$3.32 \pm .73$
CXOU J124833.2-593736	12 48 33.22	−59 37 36.8	29.6 ± 9.8	$2.23 \pm .74$

[a] The positions listed here are not corrected for any errors in the aim point of the telescope. There is an offset of about 0.″4 between the position of β Cru in the *Chandra* observation and its known optical position. So, this likely represents a systematic offset for all the source positions listed here. The statistical uncertainties in the source positions, based on random errors in the centroiding of their images in the ACIS detector are in all cases $\lesssim$0.″1.
[b] Zeroth order spectrum, background subtracted using several regions near the source to sample the background.
[c] On the range 0.5 keV $<$ hν $<$ 8 keV and, for the weak sources, based on fits to the zeroth order spectra using a power law model with interstellar absorption. For the brighter sources (β Cru and its newly discovered companion) the flux is based on two-temperature APEC model fits; discussed in §4.1 and §5.1.

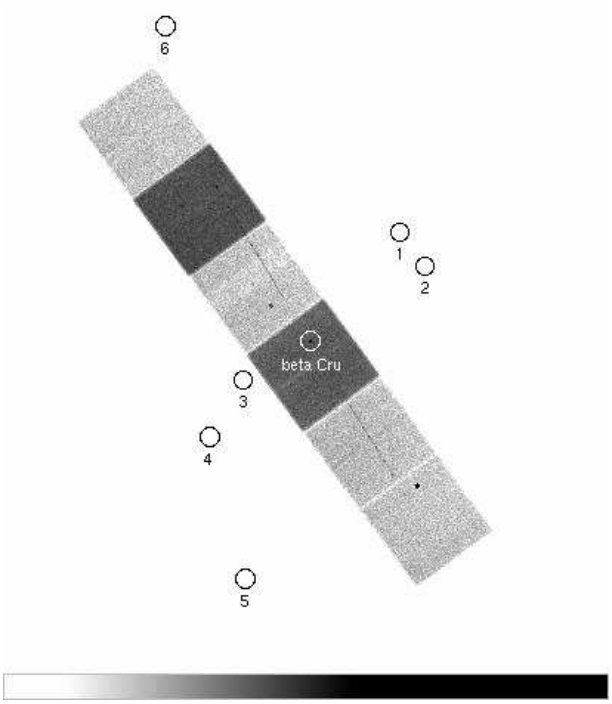

Figure 2. The orientation of the ACIS detector was such that none of the purported PMS stars identified by Park & Finley (1996) (positions shown as circles) fall on the chip. Note that the dispersed first order MEG spectrum (-1 and +1 orders) can be seen as two dark bands imaged on the ACIS chips.

3. The only other bright source in the field of view is one just 4.″0 to the southeast of β Cru at a position angle of 120 degrees, which is visibly separated from β Cru, as can be seen in Fig. 1. The position angle uncertainty is less than a degree based on the formal errors in the centroids of the two sources, and the uncertainty in the separation is less than 0.″1. We present the X-ray properties of this source in §5 and argue in §6 that it is most likely a low-mass PMS star in orbit around β Cru. The B star that dominates the optical light of the β Cru system and which is the main subject of this paper should formally be referred to as β Cru A (with spectroscopic binary components 1 and 2). The companion at a projected separation of 4 ″ will formally be known as β Cru D, since designations B and C have already been used for the purported companions listed in the Washington Double Star Catalog, mentioned in the previous section. Throughout this paper, we will refer to them simply as "β Cru" and "the companion."

We summarize the properties of all the point sources on the ACIS chips in Tab. 2. We note that the other three sources have X-ray fluxes about two orders of magnitude below those of β Cru and the newly discovered companion. They show no X-ray time variability, their spectra have mean energies of roughly 2 keV and are fit by absorbed power laws. These properties, along with the fact that they have no counterparts in the 2MASS point source catalog, indicate that they are likely AGN. We show the ACIS chips, after reprocessing, in Fig. 2. This figure demonstrates that we did not detect any of the pre-main-sequence stars seen in the *ROSAT* observation because none of them fell on the ACIS CCDs. We also note that there is no X-ray source detected at the location of the wide visual companion located 44″ from β Cru and which is no longer thought to be physically associated with β Cru (Lindroos 1985). We place a 1σ upper limit of 7 source counts in an extraction region at the position of this companion. This limit corresponds to an X-ray flux nearly three orders of magnitude below that of β Cru or its X-ray bright companion.

The position angle of the newly discovered companion is such that, for the roll angle of the *Chandra* observation, it is oriented with respect to β Cru almost exactly perpendicular to the dispersion direction of the MEG. This can be seen in Fig. 1, where parts of the rectangular extraction regions for the dispersed spectra are indicated. We were thus able to cleanly extract not just the zeroth order counts for both sources but also the first order MEG spectra for both sources. We visually inspected histograms of count rates versus pixel in the cross-dispersion direction at the locations of several lines and verified that there was no contamination of one source's spectrum by the other's. We analyze these first-order spectra as well as the zeroth-order spectra and the timing information for both sources in §4 and §5.

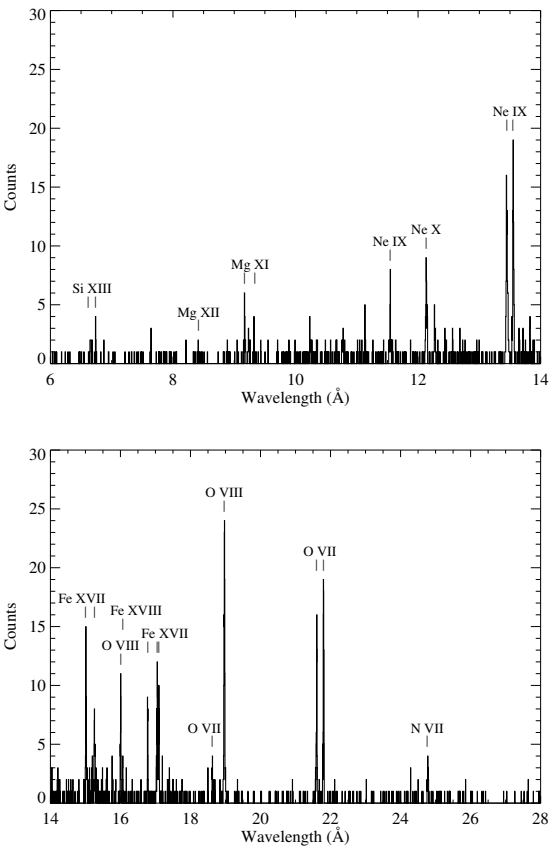

Figure 3. The MEG spectrum of β Cru, with negative and positive first orders coadded, and emission lines identified by ion. Bins are 5 mÅ wide, and each emission line spans several bins. We show a smoothed version of these same data in Fig. 5.

4 ANALYSIS OF β Cru

4.1 Spectral Analysis

The dispersed spectrum of β Cru is very soft and relatively weak. We show the co-added negative and positive first-order MEG spectra in Fig. 3, with the strong lines labeled. The softness is apparent, for example, in the relative weakness of the Ne X Lyman-α line at 12.13 Å compared to the Ne IX He$_\alpha$ complex near 13.5 Å, and indeed the lack of any strong lines at wavelengths shorter than 12 Å.

4.1.1 global thermal spectral modeling

We characterized the temperature and abundance distributions in the hot plasma on β Cru by fitting APEC thermal, optically thin, equilibrium plasma spectral emission models (Smith et al. 2001) to the both the zeroth and first order spectra. We included a model for pileup in the fit to the zeroth order spectrum (Davis 2001). There should be about 40 piled up counts in the harder portion of these data, so this correction makes a small difference in the fit. For the dispersed MEG spectrum, we adaptively smoothed the data for the fitting in ISIS. This effectively combines bins with very low count rates to improve the statistics in the continuum. We also modified the vAPEC implementation in ISIS to allow for the helium-like forbidden-to-intercombination line ratios to be free parameters (the so-called $\mathcal{G}$ parameter, which is the ratio of the forbidden plus intercombination line fluxes to the flux in the resonance line, $\mathcal{G} \equiv \frac{f+i}{r}$, was also allowed to be a free parameter). We discuss these line complexes and their diagnostic power later in this section. The inclusion of these altered line ratios in the global modeling was intended at this stage simply to prevent these particular lines from influencing the fits in ways that are not physically meaningful.

The number of free parameters in a global thermal model like APEC can quickly proliferate. We wanted to allow for a non-isothermal plasma, non-solar abundances, and thermal and turbulent line broadening (in addition to the non-standard forbidden-to-intercombination line ratios). However, we were careful to introduce new model parameters only when they were justified. So, for example, we only allowed non-solar abundances for species that have several emission lines in the MEG spectrum. And we found we could not rely solely on the automated fitting procedures in XSPEC and ISIS because information about specific physical parameters is sometimes contained in only a small portion of the spectrum, so that it has negligible effect on the global fit statistic.

We thus followed an iterative procedure in which we first fit the zeroth-order spectrum with a solar-abundance, two-temperature APEC model. We were able to achieve a good fit with this simple type of model, but when we compared the best fit model to the dispersed spectrum, systematic deviations between the model and data were apparent. Simply varying all the free model parameters to minimize the fit statistic (we used both the Cash C statistic (Cash 1979) and χ^2, periodically comparing the results for the two statistics) was not productive because, for example, the continuum in the MEG spectrum contains many more bins than do the lines, but the lines generally contain more independent information. And for some quantities, like individual abundances, only a small portion of the spectrum shows any dependence on that parameter, so we would hold other model parameters fixed and fit specific parameters on a restricted subset of the data. Once a fit was achieved, we would hold that parameter fixed and free others and refit the data as a whole.

Ultimately, we were able to find a model that provided a good fit to the combined data, both zeroth-order and dispersed spectra. The model parameters are listed in Tab. 3, and the model is plotted along with the zeroth order spectrum in Fig. 4 and the adaptively smoothed first order MEG spectrum in Fig. 5. There are some systematic deviations between the model and the data, but overall the fit quality is good, with $\chi^2_\nu = 1.09$ for the combined data. The model we present provides a better fit for the first-order MEG spectrum, which has 443 bins when we adaptively smooth it. The model gives $\chi^2_\nu = 1.00$ for the first order MEG spectrum alone, while it gives $\chi^2_\nu = 1.42$ for the zeroth order spectrum alone, which has 90 bins. We can get a good fit ($\chi^2_\nu = 1.0$) to the CCD spectrum alone with a model that has two thermal components of nearly equal strength and temperatures of 2 and 4 million K, but this model provides a substantially worse fit to the MEG data. The inability to find a formally good fit to both spectra could be the result of the instrument calibrations or it could reflect a problem with the models, but we prefer the best global fit whose param-

eters we report in Tab. 3, because the specific features that can be seen in the MEG spectrum are all well reproduced. The formal confidence limits on the fit parameters are unrealistically narrow, so we do not report them in the table. Certainly they are dominated by systematic errors, which cannot be properly accounted for in the process of assigning parameter uncertainties. The overall result, that a thermal model with a dominant temperature near 3 million K and an emission measure of $\sim 3.5 \times 10^{53}$ cm^{-3} and abundances that overall are slightly sub-solar, is quite robust.

In Fig. 5, where we show our global best-fit model superimposed on the adaptively smoothed MEG spectrum, the continuum is seen to be well reproduced and the strengths of all but the very weakest lines are reproduced to well within a factor of two. It is interesting that no more than two temperature components are needed to fit the data; the continuum shape and line strengths are simultaneously explained by a strong 2.5 million K component and a much weaker 6.5 million K component. Despite the overall agreement between the model spectrum and the data, there are some disagreements that appear systematic. The hydrogen-like lines are stronger in the model compared to the helium-like lines for the species with the highest signal-to-noise, O and Ne. This effect was seen in all models that fit the data well; it is not an artifact of the particular best-fit model we report. Adding more temperature components does not make this discrepancy go away. It is possible that this discrepancy is a sign of non-equilibrium effects, as the ionization balance of these species disagrees somewhat with the temperature derived globally from the spectral fit. Another possible hint of non-equilibrium conditions in the plasma is that the Fe XVII lines with 3s upper levels (those near 17 Å) are stronger than the best-fit model predicts they should be, while the lines with 3d upper levels (those near 15 Å) are weaker than the model predictions (Liedahl et al. 1990).

The constraints on abundances from X-ray emission line spectra are entangled with temperature effects. So, it is important to have line strength measurements from multiple ionization stages. This is strictly only true in the MEG spectrum for O and Ne, but important lines of Mg, Si, and Fe from non-dominant ionization stages would appear in the spectrum if they were strong, so the non-detections of lines of Mg XII, Si XIV, and Fe XVIII provide information about the abundances of these elements. These five elements are the only ones for which we report abundances derived from the model fitting (see Tab. 3). We allowed the nitrogen abundance to be a free parameter of the fit as well, but not report its value, as it is constrained by only one detected line in the data. Note that only O and Mg show strong evidence for sub-solar abundances, while the others are consistent with solar. The uncertainty on these abundances is difficult to reliably quantify (because of the interplay with the temperature distribution) but it is probably less than a factor of two. In general, the abundances we find are significantly closer to solar than those reported by Zhekov & Palla (2007).

In all fits we included ISM absorption assuming a hydrogen column density of 3.5×10^{19} cm^{-2}, which is consistent with the very low $E(B-V) = 0.002 \pm .011$ (Niemczura & Daszynska-Daszkiewicz 2005) and is the value determined for the nearby star HD 110956 (Fruscione et al. 1994). This low ISM column produces very little attenuation, with only a few percent of the flux absorbed even at the longest *Chandra* wavelengths. The overall X-ray flux of β Cru between 0.5 keV and 8 keV is $1.86 \pm .01 \times 10^{-12}$ ergs s^{-1} cm^{-2}, implying $L_{\rm x} = 2.6 \times 10^{30}$ ergs s^{-1}, which corresponds to $\log L_{\rm x}/L_{\rm Bol} = -7.72$.

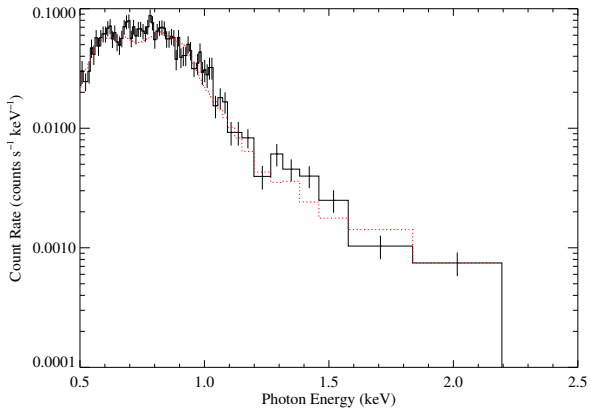

Figure 4. The best-fit two-temperature, variable abundance thermal spectral (APEC) model, corrected for pileup, superimposed on the zeroth-order spectrum. The model shown is the best-fit model fit to both the zeroth and first order spectra, with parameters listed in Tab. 3.

Table 3. Best-fit model parameters for the two-temperature APEC thermal equilibrium spectral model.

parameter	value
T_1 (K)	2.5×10^6
$\mathcal{E}M_1$ (cm^{-3})	3.3×10^{53}
T_2 (K)	6.5×10^6
$\mathcal{E}M_2$ (cm^{-3})	2.8×10^{52}
$v_{\rm turb}$ (km s^{-1})	180
$A_{\rm O}$ ($A_\odot$)	0.35
A_{Ne} ($A_\odot$)	0.78
A_{Mg} ($A_\odot$)	0.52
A_{Si} ($A_\odot$)	1.05
A_{Fe} ($A_\odot$)	0.80

4.1.2 individual emission lines: strengths and widths

Even given the extreme softness of the dispersed spectrum shown in Figs. 3, 4, and 5, the most striking thing about these data is the narrowness of the X-ray emission lines. Broad emission lines in grating spectra of hot stars are the hallmark of wind-shock X-ray emission (Cassinelli et al. 2001; Kramer et al. 2003; Cohen et al. 2006). While the stellar wind of β Cru is weaker than that of O stars, it is expected that the same wind-shock mechanism that operates in O stars is also responsible for the X-ray emission in these slightly later-type early B stars (Cohen, Cassinelli, & MacFarlane 1997). The rather narrow X-ray emission lines we see in the MEG spectrum of β Cru would thus seem to pose a severe challenge to the application of the wind-shock scenario to this early B star. We will quantify these line widths here, and discuss their implications in §6.

We first fit each emission line in the MEG spectrum individually, fitting the negative and positive first order spec-

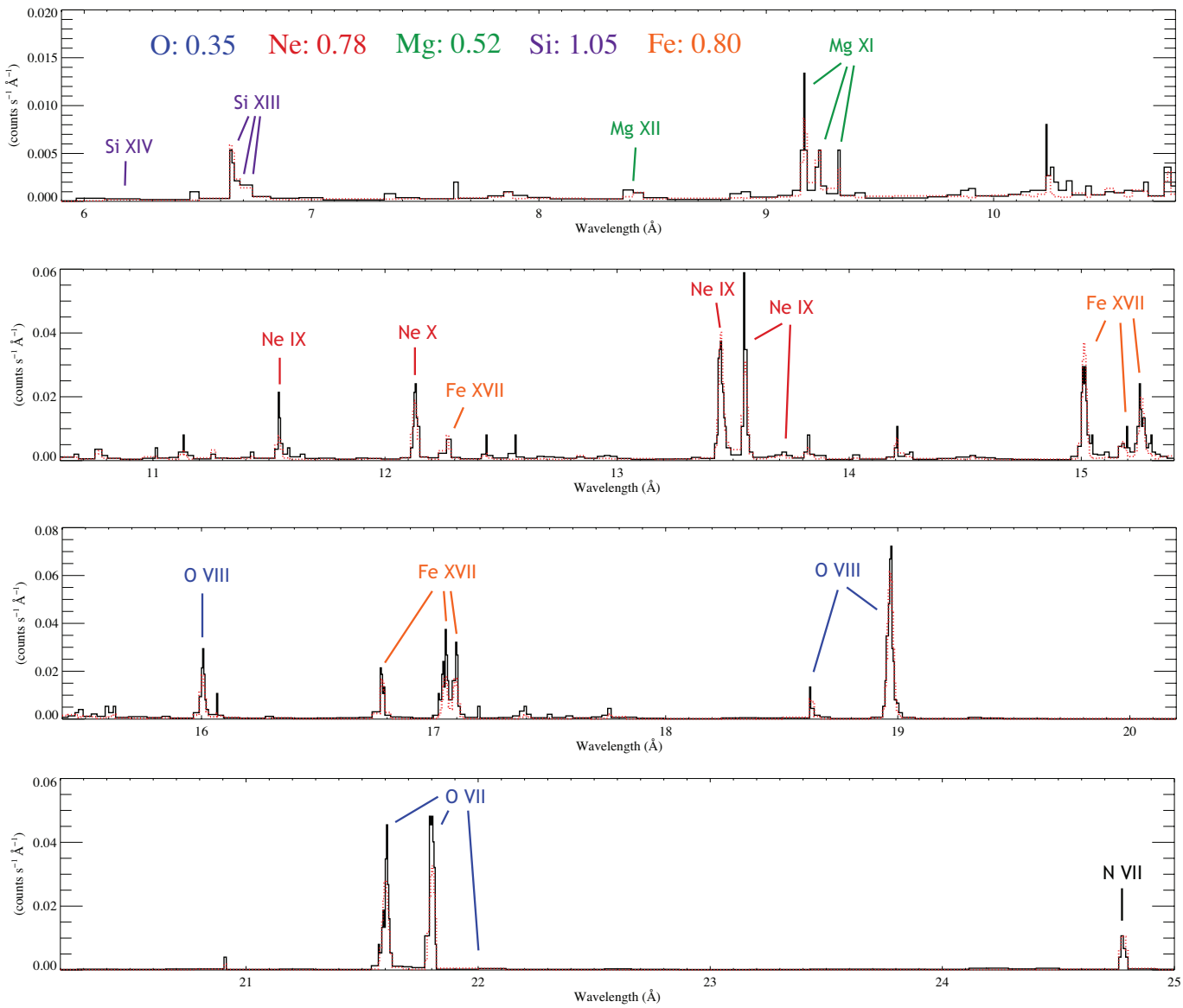

Figure 5. The best-fit two-temperature, variable abundance thermal spectral (APEC) model (dotted line; red in on-line color version; parameters listed in Tab. 3), superimposed on the adaptively smoothed co-added MEG first-order spectrum. Emission lines are labeled and color coded according to element, with the abundances of each element listed at the top of the figure. Some non-detected lines are labeled, including the forbidden line of O VII near 22.1 Å and the Lyman-alpha line of Si XIV near 6.2 Å. The nitrogen Lyman-alpha line is labeled in black, as we cannot accurately constrain its abundance because only one line is measured.

tra simultaneously (but not coadded) with a Gaussian profile model plus a power law to represent the continuum. In general, we fit the continuum near a line separately to establish the continuum level, using a power-law index of $n = 2$, ($F_\nu \propto \nu^n$, which gives a flat spectrum in F_λ vs. λ). We then fixed the continuum level and fit the Gaussian model to the region of the spectrum containing the line. We used the C statistic (Cash 1979), which is appropriate for data where at least some bins have very few counts, for all the fitting of individual lines. We report the results of these fits, and the derived properties of the lines, in Tab. 4, and show the results for the line widths in Fig. 6. Note that the half-width at half-maximum line width, for the higher signal-to-noise lines (larger and darker symbols in Fig. 6), is about 200 km s^{-1}. The weighted mean HWHM of all the lines is 143 km s^{-1}, which is indicated in the figure by the dashed line. The typical thermal width for these lines is expected to be roughly 50 km s^{-1}, so thermal broadening cannot account for the observed line widths.

To explicitly test for the presence of broadening beyond thermal broadening, when we fit the two-temperature variable abundance APEC models to the entire MEG spectrum we accounted explicitly for turbulent and thermal broadening. We found a turbulent velocity of 180 km s^{-1}, corresponding[2] to a half-width at half-maximum turbulent

[2] As implemented in ISIS, the Gaussian line profile half-width is given by $0.83\sqrt{v_{th}^2 + v_{turb}^2}$, so the HWHM that corresponds to the best-fit turbulent velocity value is 150 km s^{-1}.

Table 4. Emission Lines in the HETGS/MEG Spectrum

Ion	$\lambda_{\rm lab}$ [a] (Å)	$\lambda_{\rm obs}$ [b] (Å)	Shift (mÅ)	Half-Width[c] (mÅ)	Normalization (10^{-6} ph s^{-1} cm^{-2})	Corrected Flux [d] (10^{-15} erg s^{-1} cm^{-2})
Si XIII	6.6479 (r)	–	–	$1.7^{+3.5}_{-1.7}$	$1.06^{+0.41}_{-0.34}$	$3.15^{+1.22}_{-1.01}$
Si XIII	6.6882 (i)	–	–	1.7	$0.31^{+0.26}_{-0.17}$	$0.93^{+0.78}_{-0.51}$
Si XIII	6.7403 (f)	–	–	1.7	$0.77^{+0.33}_{-0.26}$	$2.26^{+0.97}_{-0.76}$
Mg XI	9.1687 (r)	–	–	$1.5^{+4.2}_{-1.5}$	$2.21^{+0.63}_{-0.52}$	$4.81^{+1.37}_{-1.13}$
Mg XI	9.2312 (i)	–	–	1.5	$1.25^{+0.50}_{-0.40}$	$2.70^{+1.08}_{-0.86}$
Mg XI	9.3143 (f)	–	–	1.5	$0.82^{+0.46}_{-0.30}$	$1.56^{+1.04}_{-0.71}$
Ne IX	11.5440	–	–	$1.3^{+12.8}_{-1.3}$	$6.0^{+1.3}_{-1.4}$	$10.5^{+2.2}_{-2.5}$
Ne X	12.1339	12.1331 ± 0.0019	-0.8 ± 1.9	$6.3^{+2.1}_{-2.3}$	$13.0^{+2.6}_{-1.9}$	$21.5^{+4.3}_{-3.1}$
Ne IX	13.4473 (r)	–	–	7.0 ± 1.3	$39.9^{+4.0}_{-5.2}$	$59.6^{+6.0}_{-6.6}$
Ne IX	13.5531 (i)	–	–	7.0	$37.4^{+4.2}_{-4.9}$	$55.5^{+6.1}_{-7.3}$
Ne IX	13.6990 (f)	–	–	7.0	$3.4^{+1.7}_{-1.5}$	$4.9^{+2.5}_{-2.2}$
Fe XVII	15.0140	$15.0146^{+0.0021}_{-0.0020}$	$0.6^{+2.1}_{-2.0}$	$10.0^{+2.6}_{-2.0}$	$60.6^{+5.7}_{-11.1}$	$81.1^{+7.6}_{-14.9}$
Fe XVII	15.2610	–	–	$11.7^{+3.7}_{-3.0}$	$28.1^{+5.2}_{-4.6}$	$37.1^{+6.9}_{-6.1}$
O VIII	16.0059	$16.0053^{+0.0017}_{-0.0013}$	$-0.6^{+1.7}_{-1.3}$	$0.9^{+5.1}_{-0.8}$	$32.2^{+6.1}_{-4.5}$	$40.5^{+7.7}_{-5.7}$
Fe XVIII	16.0710	–	–	$2.6^{+4.4}_{-1.6}$	$8.2^{+2.9}_{-2.5}$	$10.3^{+3.9}_{-3.2}$
Fe XVII	16.7800	$16.7756^{+0.0044}_{-0.0010}$	$-4.4^{+4.4}_{-1.0}$	$0.8^{+3.1}_{-0.8}$	$31.8^{+5.9}_{-5.7}$	$38.3^{+7.1}_{-6.9}$
Fe XVII	17.0510	$17.0477^{+0.0020}_{-0.0017}$	$-3.3^{+2.0}_{-1.7}$	$8.8^{+1.5}_{-1.7}$	$67.3^{+6.4}_{-5.8}$	$78.4^{+9.0}_{-5.5}$
Fe XVII	17.0960	$17.0938^{+0.0022}_{-0.0016}$	$-2.2^{+2.2}_{-1.6}$	8.8	$53.2^{+6.3}_{-6.5}$	$62.9^{+7.4}_{-7.7}$
O VII	18.6270	–	–	$3.9^{+12.4}_{-3.9}$	$21.1^{+8.3}_{-5.9}$	$22.9^{+9.0}_{-6.4}$
O VIII	18.9689	$18.9671^{+0.0014}_{-0.0011}$	$-1.8^{+1.4}_{-1.1}$	10.4 ± 1.3	260^{+21}_{-24}	278^{+22}_{-26}
O VII	21.6015 (r)	$21.6016^{+0.0018}_{-0.0017}$	$-0.1^{+1.8}_{-1.7}$	11.0 ± 1.8	295 ± 34	279 ± 30
O VII	21.8038 (i)	$21.7982^{+0.0012}_{-0.0009}$	$-5.6^{+1.2}_{-0.9}$	$5.4^{+1.6}_{-1.7}$	414^{+42}_{-41}	389^{+39}_{-39}
O VII[e]	22.0977 (f)	–	–	–	< 19.3	< 17.9
N VII	24.7810	–	–	$7.7^{+3.7}_{-3.2}$	92 ± 21	75^{+18}_{-16}

[a] Lab wavelength taken from APED (Smith et al. 2001). For closely spaced doublets (e.g. Lyman-alpha lines) an emissivity-weighted mean wavelength is reported. The resonance (r), intercombination (i), and forbidden (f) lines of Si, Mg, Ne, and O are indicated.
[b] If no value is given, then this parameter was held constant at the laboratory value when the fit was performed.
[c] For closely spaced lines, such as the He-like complexes, we tied the line widths together but treated the common line width as a free parameter. This is indicated by identical half-width values and formal uncertainties listed on just the line with the shortest wavelength.
[d] Corrected for an ISM column density of $N_H = 3.5 \times 10^{19}$ cm^{-2} using Morrison & McCammon (1983) photoelectric cross sections as implemented in the XSPEC model (*wabs*).
[e] The normalization and corrected flux values for the forbidden line of O VII are based on the 68% confidence limit for a Gaussian line profile with a fixed centroid and a fixed width (of 7 mÅ). The data are consistent with a non-detection of this line.

velocity of 150 km s^{-1}, from a single global fit to the spectrum. We will characterize the overall line widths as $HWHM$ = 150 km s^{-1}/ for the rest of the paper. The thermal velocity for each line follows from the fitted temperature(s) and the atomic mass of the parent ion. This turbulent broadening is consistent with what we find from the individual line fitting, as shown in Fig. 6. We also find and a shift of -20 km s^{-1} from a single global fit to the spectrum. We note that this 20 km s^{-1} blue shift of the line centroids is not significant, given the uncertainty in the absolute wavelength calibration of the HETGS (Marshall et al. 2004).

Because the emission lines are only barely resolved, there is not a lot of additional information that can be extracted directly from their profile shapes. However, because the working assumption is that this line emission arises in the stellar wind, it makes sense to fit line profile models that are specific to stellar wind X-ray emission, and see if they are at least consistent with the data. We thus fit the empirical wind-profile X-ray emission line model developed by Owocki & Cohen (2001) to each line, again with a power-law continuum model included. This wind-profile model, though informed by numerical simulations of line-driven instability (LDI) wind shocks (Owocki et al. 1988; Cohen et al. 1996; Feldmeier et al. 1997), is phenomenological, and only depends on the spatial distribution of X-ray emitting plasma, its assumed kinematics (described by a beta velocity law in a spherically symmetric wind), and the optical depth of the bulk cool wind. For the low-density wind of β Cru, it is safe to assume that the wind is optically thin to X-rays. And once a velocity law is specified, the only free parameter of this wind-profile model - aside from the normalization - is the minimum radius, $R_{\rm min}$, below which there is assumed to be no X-ray emission. Above $R_{\rm min}$, the X-ray emission is assumed to scale with the square of the mean wind density.

When we fit these wind-profile models, we had to decide what velocity law to use for the model. From CAK (Castor, Abbott, & Klein 1975) theory, we expect a terminal velocity of roughly 2000 km s^{-1}. The β parameter of the standard wind velocity law governs the wind acceleration according to $v = v_\infty(1 - {\rm R}_*/{\rm r})^\beta$ so that large values of β give more gradual accelerations. Typically $\beta \approx 1$. When

we fit the wind-profile model with $v_\infty = 2000$ km s^{-1} and $\beta = 1$ to the stronger lines, we could only fit the data if $R_{\rm min} < 1.1$ R$_*$. This puts nearly all of the emission at the base of the wind (because of the density-squared weighting of X-ray emissivity and the $v^{-1}r^{-2}$ dependence of density), which is unrealistic for any type of wind-shock scenario, but which is the only way to produce the relatively narrow profiles in a model with a large wind terminal velocity. This quantitative result verifies the qualitative impression that the relatively narrow emission lines in the MEG spectrum are inconsistent with a standard wind-shock scenario in the context of a fast wind.

However, although the theoretical expectation is for a fast wind with a terminal velocity of roughly 2000 km s^{-1}, the UV wind line profiles observed with *IUE* tell a different story. The UV line with the strongest wind signature is the C IV doublet at 1548,1551 Å, which shows a blue edge velocity of only 420 km s^{-1} (Prinja 1989). We show this line in Fig. 7. The C III line shows no wind broadening and the Si IV line shows a slightly weaker wind signature than the C IV feature. Certainly the terminal velocity of the wind could be significantly higher than this, with the outer wind density being too low to cause noticeable absorption at high velocities. However, because the empirical evidence from these UV wind features indicates that the terminal velocity of the wind may actually be quite low, we refit the strong lines in the MEG spectrum with the wind-profile model, but this time using a terminal velocity of 420 km s^{-1}. The fits were again statistically good, and for these models, the fitted values of $R_{\rm min}$ were generally between 1.3 R$_*$ and 1.5 R$_*$, which are much more reasonable values for the onset radius of wind-shock emission.

We also considered a constant-velocity model ($\beta = 0$), where the X-rays perhaps are produced in some sort of termination shock. For these fits, $R_{\rm min}$ hardly affects the line width, so we fixed it at 1.5 R$_*$ and let the (constant) terminal velocity, v_∞, be a free parameter. For the seven lines or line complexes with high enough signal-to-noise to make this fitting meaningful, we found best-fit velocities between 270 km s^{-1} and 300 km s^{-1} for five of them, with one having a best-fit value lower than this range and one line having a best-fit value higher than this range. The average wind velocity for these seven lines is $v_\infty = 280$ km s^{-1}. All in all, the emission line widths are consistent[3] with a constant-velocity outflow of 280 km s^{-1}, and are inconsistent with a wind-shock origin in a wind with a terminal velocity of 2000 km s^{-1}. The lines are narrower than would be expected even for a wind with a terminal velocity not much greater than the observed C IV blue edge velocity, $v = 420$ km s^{-1} (based on our $\beta = 1$ fits as well as the $\beta = 0$ fits). The X-ray emitting plasma must be moving significantly slower than the bulk wind. In Fig. 8 we show the best-fit constant velocity model ($v_\infty = 280$ km s^{-1}) superimposed on the Fe XVII line at 15.014 Å, along with the higher velocity model based on the theoretically expected terminal velocity, which clearly does not fit the data well. We also compare the best-fit wind-profile model to a completely narrow profile in this figure. The modestly wind-broadened profile that provides the best fit is preferred over the narrow profile at the 99% confidence level.

[3] The measured line widths (of ≈ 150 km s^{-1} derived from both the Gaussian fitting and the global thermal spectral modeling) are expected to be somewhat smaller than the modeled wind velocity, as some of the wind, in a spherically symmetrical outflow, will be moving tangentially to the observer's line of sight. So, a spherically symmetric, constant velocity wind with $v_\infty = 280$ km s^{-1} is completely consistent with emission lines having HWHM values of 150 km s^{-1}.

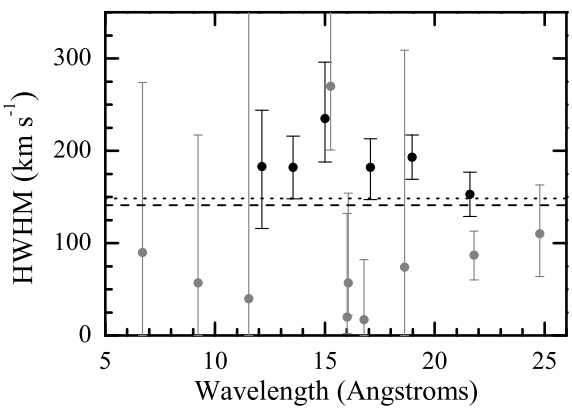

Figure 6. Half-width at half-maximum line widths derived from fitting Gaussian line-profile models to each individual line in the MEG first-order spectrum. The strongest, well behaved, isolated lines are indicated with darker symbols. The lower signal-to-noise, blended, or otherwise less reliable lines are shown in gray. 68% confidence limit error bars are shown for all the lines. The weighted mean HWHM velocity for all the lines is indicated by the dashed horizontal line, while the HWHM that corresponds to the turbulent velocity derived from the global spectral fit is indicated by the dotted horizontal line (recall that $v_{turb} = 180$ km s^{-1} corresponds to a half width at half maximum of 150 km s^{-1}).

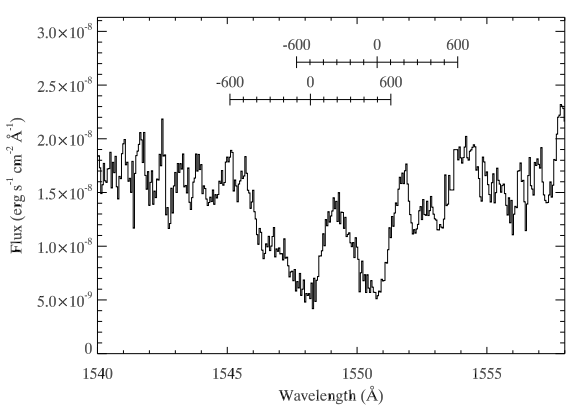

Figure 7. The C IV resonance doublet from several coadded *IUE* observations taken from the archive. A velocity scale in the frame of the star is shown above the data. These lines show the characteristic blue-shifted absorption that is expected from a stellar wind, but the lines are both weak compared to theoretical expectations and also much less wind broadened.

Table 5. Helium-like complexes

Ion	$\mathcal{R} \equiv f/i^a$	$\lambda_{\rm UV}$ (Å)^b	H_ν (ergs s^{-1} cm^{-2} Hz^{-1})^c	$R_{\rm fir}$ (R$_*$)^d	$R_{\rm min}$ (R$_*$)^e	$\mathcal{G} \equiv \frac{(f+i)}{r}$
Ne IX	$0.09 \pm .05$	1248, 1273	1.35×10^{-3}	$2.9^{+0.7}_{-1.0}$	$1.37^{+.18}_{-.02}$	1.05
Mg XI	$0.65 \pm .44$	998, 1034	1.39×10^{-3}	$3.2^{+1.4}_{-1.5}$	$1.80^{+1.33}_{-0.45}$	1.01

[a] From Gaussian fitting. The values we obtain from the APEC global fitting within ISIS are consistent with the f/i values reported here.
[b] The UV wavelengths at which photoexcitation out of the upper level of the forbidden line occurs.
[c] The assumed photospheric Eddington flux at the relevant UV wavelengths, based on the TLUSTY model atmosphere, which we use to calculate the dependence of f/i on the radius of formation, $R_{\rm fir}$.
[d] Formation radius using eqn. (1c) of Blumenthal et al. (1972) and eqn. (3) of Leutenegger et al. (2006), and based on the f/i values in the second column.
[e] From wind profile fitting, assuming $\beta = 1$ and letting v_∞ be a free parameter. The $\mathcal{G}$ values in the last column also come from the profile fitting.

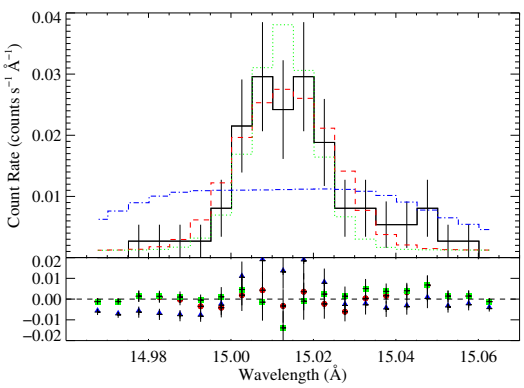

Figure 8. The Fe XVII line at 15.014 Å with three different wind profile models. The dashed line (red in on-line color version) is a constant-velocity wind model with $v_\infty = 280$ km s^{-1} (the best-fit value for a constant outflow velocity, which produces emission lines with $v_{HWHM} \approx 150$ km s^{-1}). The model with $v_\infty = 2000$ km s^{-1}, $\beta = 1$, and $R_{\rm min} = 1.5$ R$_*$ is represented by the dot-dash line (blue in on-line color version). An infinitely narrow model is shown as the dotted line (green in on-line color version). The residuals for each model fit are shown in the lower panel, as red circles for the global best-fit, modestly broadened ($v_\infty = 280$ km s^{-1}) model, green squares for the narrow profile model, and blue triangles for the broad wind model. The wind model with the higher velocity ($v_\infty = 2000$ km s^{-1}) clearly does not provide a good fit, while the narrower constant velocity ($v_\infty = 280$ km s^{-1}) wind model does. And while the very narrow model cannot be absolutely ruled out, the $v_\infty = 280$ km s^{-1} model is preferred over it with a high degree of significance. All the models shown here have been convolved with the instrumental response function.

4.1.3 helium-like forbidden-to-intercombination line ratios

The final spectral diagnostic we employ is the UV-sensitive forbidden-to-intercombination line ratio of helium-like ions. These two transitions to the ground-state have vastly different lifetimes, so photoexcitation out of the 1s2s ^{3}S$_1$ state, which is the upper level of the forbidden line, to the 1s2p ^{3}P$_{1,2}$ state, which is the upper level of the intercombination line, can decrease the forbidden-to-intercombination line ratio, $\mathcal{R} \equiv f/i$. Because the photoexcitation rate depends on the local UV mean intensity, the f/i ratio is a diagnostic of the distance of the X-ray emitting plasma from the photosphere. This diagnostic has been applied to many of the hot stars that have *Chandra* grating spectra, and typically shows a source location of at least half a stellar radius above the photosphere. Recently, Leutenegger et al. (2006) have shown that the f/i ratios from a spatially distributed X-ray emitting plasma can be accounted for self-consistently with the line profile shapes in four O stars, providing a unified picture of wind-shock X-ray emission on O stars.

We derive a single characteristic radius of formation, $R_{\rm fir}$, for each complex by calculating the dependence of the f/i ratio on the distance from the photosphere, using a TLUSTY model atmosphere (Lanz & Hubeny 2007). We used the formalism of Blumenthal et al. (1972), equation (1c), ignoring collisional excitation out of the ^{3}S$_1$ level, and explicitly expressing the dependence on the dilution factor, and thus the radius, as in equation (3) in Leutenegger et al. (2006). The measurement of f/i from the data can then be used to constrain the characteristic formation radius, $R_{\rm fir}$.

The lower-Z species like oxygen do not provide any meaningful constraints, as is the case for O stars, and there are not enough counts in the Si XIII complex to put any meaningful constrains on the source location. Only the Ne IX and Mg XI complexes provide useful constraints. For both Ne IX and Mg XI we find $R_{\rm fir} \approx 3 \pm 1R_*$. Of course, the line-emitting plasma is actually distributed in the wind, and so we also fit the same modified Owocki & Cohen (2001) wind profile model that Leutenegger et al. (2006) used to fit a distributed X-ray source model to the He-like complexes, accounting simultaneously for line ratio variations and wind-broadened line profiles. With the wind velocity law and $\mathcal{G} \equiv \frac{f+i}{r}$ as free parameters, strong constraints could not be put on the models. Typically, these distributed models of f/i gave onset radii, $R_{\rm min}$, that were quite a bit lower than $R_{\rm fir}$. This is not surprising, because a distributed model will inevitably have some emission closer to the star than $R_{\rm fir}$ to compensate for some emission arising at larger radii. We list the results of such a wind-profile fit to the He-like complexes in Tab. 5 along with the $R_{\rm fir}$ values. The two helium-like complexes and the best-fit models are shown in Figs. 9 and 10, along with the modeling of the f/i ratios and the characteristic formation radii, $R_{\rm fir}$. We note that the data rule out plasma right at the photosphere only at the 68% confidence level. Finally, we note that while iron line blending does not appear to be a problem for the Ne IX

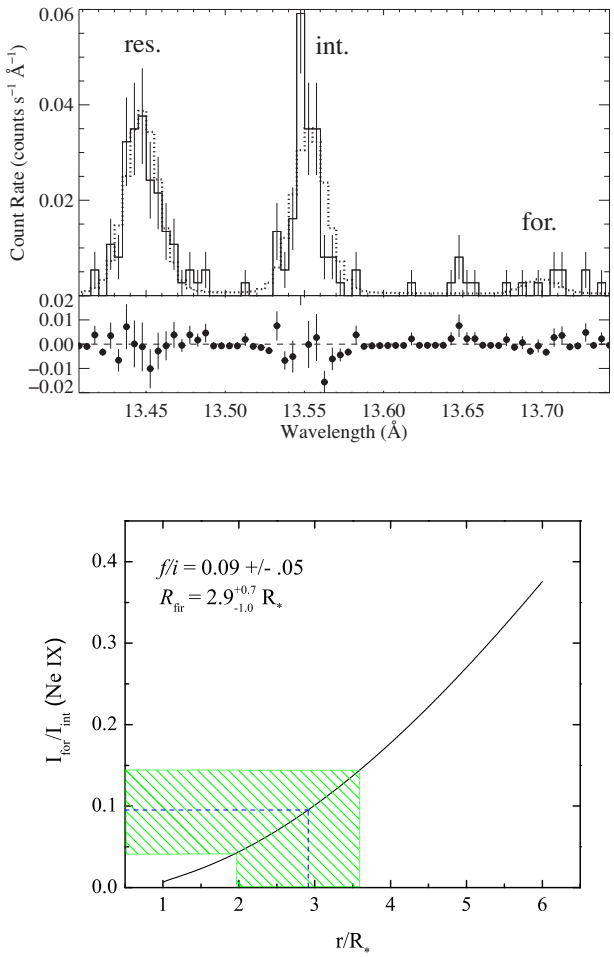

Figure 9. The Ne IX resonance-intercombination-forbidden complex in the co-added MEG data, with the best-fit three-Gaussian model overplotted (top). The constraints on the measured f/i ratio ($0.09 \pm .05$), from the fit shown in the top panel, are indicated by the cross-hatched area's intersection with the y-axis (bottom). The solid black curve is the model for the line ratio, as a function of radius. The cross-hatched region's intersection with the model defines the 68% confidence limit on r/R_*. The dashed line represents the best-fit value, $f/i = 0.09$, and the corresponding $R_{\mathrm{fir}} = 2.9$ R$_*$.

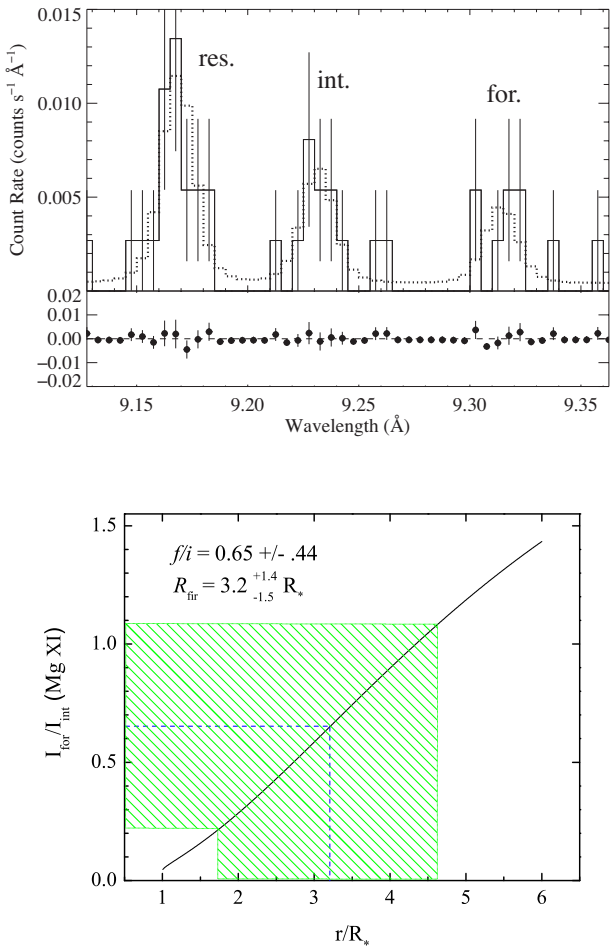

Figure 10. The Mg XI resonance-intercombination-forbidden complex in the co-added MEG data, with the best-fit wind-profile models overplotted (top). The constraints on the formation radius, R_{fir}, are shown below.

complex, there are hints of DR satellite lines of neon in the data.

4.2 Time Variability Analysis

We first examined the *Chandra* data for overall, stochastic variability. Both a K-S test applied to the unbinned photon arrival times and a χ^2 fitting of a constant source model to the binned light curve showed no evidence for variability in the combined zeroth order and first order spectra. This is to be expected from wind-shock X-rays, which generally show no significant variability. This is usually interpreted as evidence that the X-ray emitting plasma is distributed over numerous spatial regions in the stellar wind (Cohen, Cassinelli, & MacFarlane 1997). Separate tests of the hard ($h\nu > 1$ keV) and soft ($h\nu < 1$ keV) counts showed no evidence for variability in the soft data, but some evidence for variability (K-S statistic implies 98% significance) in the hard data.

Because β Cru is a β Cephei variable, we also tested the data for periodic variability. Both the changes in the star's effective temperature with phase and the possible effects of wave leakage of the pulsations into the stellar wind could cause the X-ray emission, if it arises in wind shocks, to show a dependence on the pulsational phase (Owocki & Cranmer 2002). Our *Chandra* observation covers about four pulsations periods. To test for periodic variability, we used a variant of the K-S test, the Kuiper test (Paltani 2004), which is also applied to unbinned photon arrival times. To test the significance of a given periodicity, we converted the photon arrival times to phase and formed a cumulative distribution of arrival phases from the events table. We then calculated the Kuiper statistic and its significance for that particular period. By repeating this process for a grid of test periods, we identified significant periodicities in the data.

When we applied this procedure to all the zeroth-order and first-order counts we did not find any significant periodicities. However, applying it only to the hard counts pro-

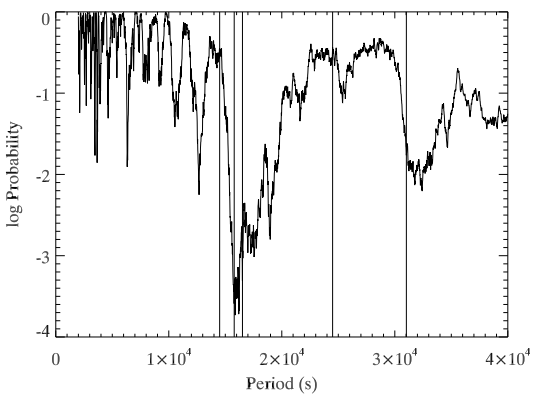

Figure 11. Rejection probability (significance level increasing downward) of assumed period, according to the Kuiper statistic. The five known optical pulsation periods (Aerts et al. 1998; Cuypers et al. 2002) are indicated by the vertical lines. The primary pulsation period is the third of these.

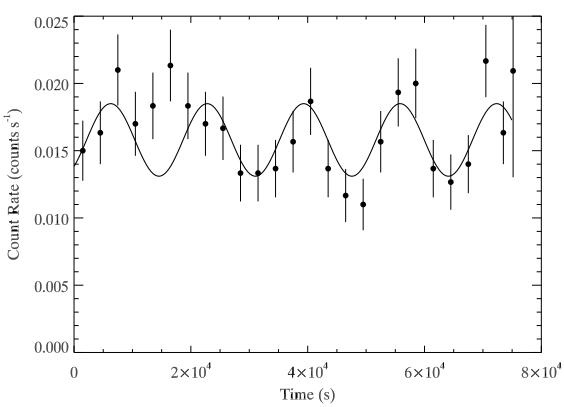

Figure 12. The light curve of the hard counts in the zeroth and first order spectra of the primary, along with the best-fit sinusoidal model.

duced a significant peak near the primary and tertiary optical pulsation periods (f_1 and f_3) of 4.588 hours and 4.386 hours (Aerts et al. 1998), as shown in Fig. 11. This peak is significant at the 99.95% level. It is relatively broad as the data set covers only about four cycles of the pulsation, so it is consistent with both pulsation modes, but not with the secondary (f_2) mode (Aerts et al. 1998). No significant periods are found in the soft bandpass, despite the higher signal-to-noise there. To quantify the level of periodic variability we found in the hard counts, we made a binned light curve from these counts and fit a sine wave with a period of 4.588 hours, leaving only the phase and the amplitude as free parameters. We find a best-fit amplitude of 18%. We show the light curve and this fit in Fig. 12 and note that there appears to be some additional variability signal beyond the strictly periodic component. We also note that there is a phase shift between the times of maximum X-ray and optical light, of about a quarter period ($\Delta\phi = 0.27 \pm .04$), with the X-rays lagging behind the optical variability. To make this assessment, we compared the time of maximum X-ray

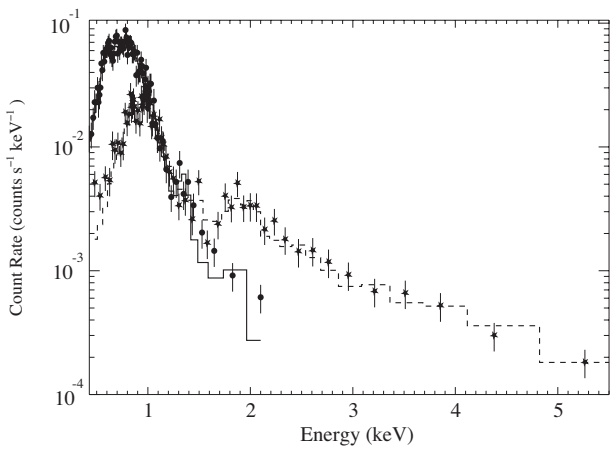

Figure 13. The zeroth order spectrum of the companion (stars) is shown along with that of β Cru (circles). The companion's spectrum is significantly harder, and is well-fit by a two-temperature thermal model with component temperatures several times higher than those found for β Cru.

light from the sinusoidal fitting shown in Fig. 12 to the time of maximum optical light in the WIRE data, based on just the primary pulsation mode (Cuypers 2007, private communication). We note that $\phi = 0.25$ corresponds to the maximum blue shift in the radial velocity variability of β Cephei stars (Mathias et al. 1992).

5 ANALYSIS OF THE POSSIBLE COMPANION

We subjected the newly discovered companion to most of the same analyses we have applied to β Cru, as described in the previous section. The exceptions are the wind-profile fitting, which is not relevant for the unresolved lines in the companion's spectrum, and the tests for periodic variability, since none is expected.

Our working hypothesis is that the X-ray bright companion is a low-mass pre-main-sequence star, similar to those found in the *ROSAT* pointing (Park & Finley 1996; Feigelson & Lawson 1997; Alcalá et al. 2002). In the following two subsections, we marshal evidence from the spectral and time-variability properties to address this hypothesis.

5.1 Spectral Analysis

The spectrum of the companion is significantly harder than that of β Cru. This can be seen in both the zeroth-order spectrum (see Fig. 13 and the on-line color version of Fig. 1) and the dispersed spectrum (see Fig. 14). The dispersed spectrum has quite poor signal-to-noise, as the hardness implies fewer counts than β Cru despite their relatively similar X-ray fluxes.

We fit a two-temperature optically thin coronal equilibrium spectral model to the zeroth order spectrum of the companion. As we did for the primary, we compared the best-fit model's predictions to the MEG spectrum and found good agreement. This source is significantly harder than β Cru, as indicated by the model fit, which has component temperatures of 5.6 and 23 million K. The emis-

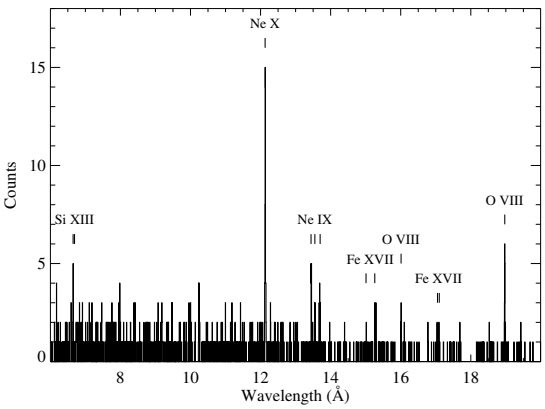

Figure 14. The co-added MEG negative and positive first order spectrum of the companion. The emission is clearly thermal. Its properties are consistent with *Chandra* HETGS spectra of active late-type stars.

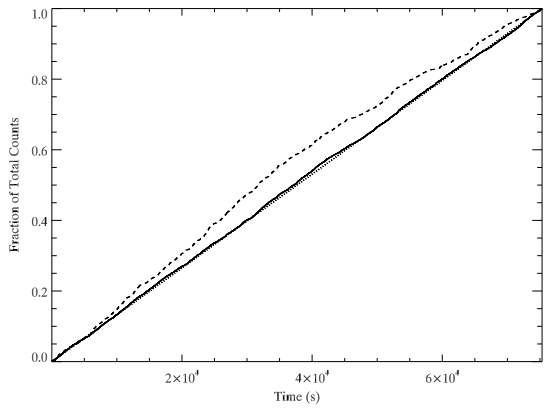

Figure 15. The cumulative distribution functions of the arrival times of all zeroth and MEG first order counts for the companion (dashed line), compared to β Cru (solid line). A constant model is also shown (straight, dotted line) for comparison. The companion is clearly much more variable than is β Cru. Note that these empirical distribution functions (EDFs) are the basis of the K-S and Kuiper statistics that we use to test the data for variability.

sion measures of the two components are 2.1×10^{52} cm^{-3} and 4.3×10^{52} cm^{-3}, respectively, yielding an X-ray flux of $5.73 \pm .06 \times 10^{-13}$ ergs s^{-1} cm^{-2}, corrected for ISM absorption using the same column density that we used for the analysis of the spectrum of β Cru. This flux implies $L_{\rm x} = 8.0 \times 10^{29}$ ergs s^{-1}. No significant constraints can be put on the abundances of the X-ray emitting plasma from fitting the *Chandra* data.

Unlike β Cru, the companion has lines that are narrow – unresolved at the resolution limit of the HETGS. This, and the hardness of the spectrum, indicates that the companion is consistent with being an active low-mass main-sequence star or pre-main-sequence stars.

The f/i ratios that provided information about the UV mean intensity and thus the source distance from the photosphere in the case of β Cru can be used in coronal sources as a density diagnostic. The depopulation of the upper level of the forbidden line will be driven by collisions, rather than photoexcitation, in the case of cooler stars. Some classical T Tauri stars (cTTSs) have shown anomalously low f/i ratios compared to main sequence stars and even weak-line T Tauri stars (wTTSs) (Kastner et al. 2002; Schmitt et al. 2005). The best constraint in the companion's spectrum is provided by Ne IX, which has $f/i = 2.2 \pm 1.1$. This value is consistent with the low-density limit of $f/i = 3.0$ (Porquet & Dubau 2000), which is typically seen in wTTSs and active main sequence stars but is sometimes altered in cTTSs. Using the calculations in Porquet & Dubau (2000), we can place an upper limit on the electron density of $n_{\rm e} \approx 10^{12}$ cm^{-3}, based on the 1σ lower limit of the f/i ratio.

5.2 Time Variability Analysis

The companion is clearly much more variable than is β Cru. The K-S test of the unbinned photon arrival times shows significant variability in all energy bands, though the significance is higher in the hard X-rays ($h\nu > 1$ keV). The binned light curve also shows highly significant variability, again with the null hypothesis of a constant source rejected for the overall data, and both the soft and hard counts, separately. In Fig. 15 we show the empirical distribution function (EDF) of the photon arrival times. It can be seen that the variability is much more dramatic than that of β Cru.

The morphology of the EDF indicates an overall decrease in the count rate as the observation progressed, which is seen clearly in the binned light curve shown in Fig. 16. The short rise followed by a steady decline of nearly 50% in the X-ray count rate over the remainder of the observation is qualitatively consistent with flare activity seen in late-type PMS stars (Favata et al. 2005), although the rise is not as rapid as would be expected for a single, large flare. We examined the spectral evolution of the companion during this decay, and there is mild evidence for a softening of the spectrum at late times, but not the dramatic spectral evolution expected from a cooling magnetic loop after a flare. For example, the hardness ratio (the difference between the count rate above 1 keV and below 1 keV, normalized by the total count rate) is shown in Fig. 17. There is a mild preference for a negative slope over a constant hardness ratio (significant at the 95% level), but with the data as noisy as they are, a constant hardness ratio cannot be definitively ruled out.

6 DISCUSSION AND CONCLUSIONS

Although it is very hot and luminous, β Cru has a *Chandra* spectrum that looks qualitatively quite different from those of O stars, with their significantly Doppler broadened X-ray emission lines. Specifically, the emission lines of β Cru are quite narrow, although they are resolved in the MEG, with half-widths of ~ 150 km s^{-1}. These relatively narrow lines are incompatible with the wind-shock scenario that applies to O stars if the wind of β Cru has a terminal velocity close to the expected value of $v_\infty \approx 2000$ km s^{-1}. They are consistent with a spherically symmetric outflow with a constant velocity of $v_\infty = 280$ km s^{-1} though, with the half-width of the observed lines being smaller (~ 150 km s^{-1}) because

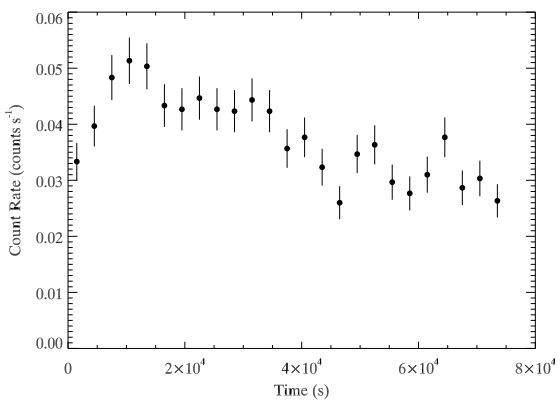

Figure 16. The binned light curve of the secondary, including all zeroth- and first-order counts.

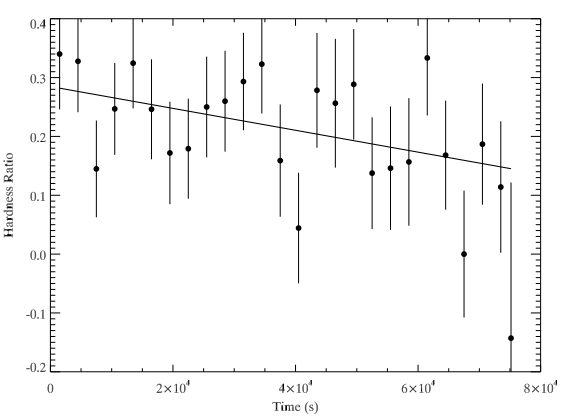

Figure 17. The hardness ratio, defined as $HR \equiv \frac{CR(>1\mathrm{keV})-CR(<1\mathrm{keV})}{CR(>1\mathrm{keV})+CR(<1\mathrm{keV})}$, where the CR denotes the count rate in the combined zeroth order and first order (MEG) data, over the indicated photon energy ranges. We fit a linear function to the data, and find $\chi^2 = 25$ for 24 degrees of freedom for a constant model (slope of zero), so a constant source model cannot be rejected outright. However, the best-fit slope of -1.9×10^{-6} cts s^{-2} gives $\chi^2 = 20$, which is a statistically significant improvement.

not all of the outflow is moving radially with respect to the observer.

If the wind terminal velocity is significantly less than 2000 km s^{-1} – perhaps just a few hundred km s^{-1} above the 420 km s^{-1} maximum absorption velocity shown by the strongest of the observed UV wind lines – a wind-shock origin of the X-ray emission is possible, but still difficult to justify. One wind-shock scenario that we have considered relies on the fact that the low-density wind of β Cru should take a long time to cool once it is shock heated. If a large fraction of the accelerating wind flow passes through a relatively strong shock front at $r \approx 1.5$ R$_*$, where the pre-shock wind velocity may be somewhat less than 1000 km s^{-1}, it could be decelerated to just a few 100 km s^{-1}, explaining the rather narrow X-ray emission lines. Similar onset radii are seen observationally in O stars (Kramer et al. 2003; Cohen et al. 2006; Leutenegger et al. 2006). The hottest plasma component from the global thermal spectral modeling requires a shock jump velocity of roughly 700 km s^{-1}, with the dominant cooler component requiring a shock jump velocity of roughly 400 km s^{-1}. Note that the sum of the post-shock velocity (which we associate with the X-ray emitting plasma) and the shock-jump velocity is equal to the pre-shock velocity in the frame of the shock front.

The f/i ratios of Ne IX and Mg XI indicate that the hot plasma is either several stellar radii from the photosphere or distributed throughout the wind starting at several tenths of a stellar radius. This is broadly consistent with this scenario of an X-ray emitting outer wind. The lack of overall X-ray variability would also be broadly consistent with this quasi-steady-state wind-shock scenario. And the periodic variability seen in the hard X-rays could indicate that the shock front conditions are responding to the stellar pulsations, while the lack of soft X-ray variability would be explained if the softer X-rays come from cooling post-shock plasma in which the variability signal has been washed out.

The overall level of X-ray emission is quite high given the modest wind density, which is a problem that has been long-recognized in early B stars (Cohen, Cassinelli, & MacFarlane 1997). A large fraction of the wind is required to explain the X-ray emission. Elaborating on the scenario of a shock-heated and inefficiently cooled outer wind, we can crudely relate the observed X-ray emission measure to the uncertain mass-loss rate.

Assuming a spherically symmetric wind in which the X-rays arise in a constant-velocity post-shock region that begins at a location, R_0, somewhat above the photosphere; say $R_0 \approx 1.5$ (in units of R$_*$), we can calculate the emission measure available for X-ray production from

$$\mathcal{E}M \equiv \int n_{\rm e} n_{\rm H} dVol = \int_{R_0}^{\infty} n_{\rm e} n_{\rm H} 4\pi r^2 dr.$$

Again assuming spherical symmetry and a smooth flow with a constant velocity for $r > R_0$, we have

$$\mathcal{E}M = 1.3 \times 10^{54} \frac{\dot{M}_{-9}^2}{R_0 v_{100}^2} \quad (\mathrm{cm}^{-3})$$

for the emission measure of the entire wind above $r = R_0$, where $\dot{M}_{-9}$ is the mass-loss rate in units of 10^{-9}M$_\odot$ yr^{-1} and v_{100} is the wind velocity in units of 100 km s^{-1}. Equating this estimate of the available emission measure to that which is actually observed in the data, 3.5×10^{53} cm^{-3}, we get

$$\dot{M}_{-9} = \sqrt{\frac{\mathcal{E}M}{1.3 \times 10^{54}} R_0 v_{100}^2} \approx 1$$

for $R_0 \approx 1.5$ and $v = 280$ km s^{-1} ($v_{100} = 2.8$), which is the velocity obtained from fitting the line widths in the MEG spectrum. Thus a mass-loss rate of order 10^{-9}M$_\odot$ yr^{-1} is consistent with the observed X-ray emission measure[4]. This

[4] We hasten to point out that our analysis ignores the possibility that less than the entire wind volume beyond $r = R_0$ is X-ray emitting. Certainly a filling factor term could multiply the mass-loss rate in the expression for the emission measure. Ignoring such a finite filling factor would lead us to underestimate the mass-loss rate. However, another simplification we have made here involves the assumption of a smooth, spherically symmetric distribution.

type of simple analysis relating the observed X-ray emission measure in early B stars to their mass-loss rate in the context of shock heating and inefficient radiative cooling in the outer wind was applied to *ROSAT* observations of the early B giants ϵ and β CMa by Drew et al. (1994), who, like we have here, found lower mass-loss rates than expected from theory. A downward revision in the mass-loss rates of early B stars might not be surprising given recent work indicating that the mass-loss rates of O stars have been overestimated (Bouret et al. 2005; Fullerton et al. 2006; Cohen, Leutenegger, & Townsend 2007).

Given the estimated mass-loss rate of $\dot{M} \approx 10^{-9}$ $M_\odot$ yr^{-1} for β Cru, we can assess the cooling time, or cooling length, of the purported wind shocks. A crude estimate of the cooling time and length of shock-heated wind material can be made by comparing the thermal energy content of the post-shock plasma,

$$E_{\rm th} = \frac{3}{2} nkT \approx 0.1 \quad (\text{ergs cm}^{-3})$$

to the radiative cooling rate,

$$\frac{dE}{dt} = n^2 \Lambda \approx 5 \times 10^{-7} \quad (\text{ergs s}^{-1}\ \text{cm}^{-3}).$$

These numbers come from taking expected values of the wind density based on the assumptions of spherical symmetry of the wind and a constant outflow velocity,

$$n = 6 \times 10^8 \frac{\dot{M}_{-9}}{R^2 v_{100}} \quad (\text{cm}^{-3}),$$

where R is the radial location in units of stellar radii. Using $v_{100} = 2.8$ and $\dot{M}_{-9} = 1$, the density is just $n \approx 10^8$ cm^{-3} at $R = 1.5$. We use temperatures of $T = 2.5$ and 6.5×10^6 K, given by the spectral fitting discussed in §4.1, assuming that some of the softer thermal component is produced directly by shock heating since the emission measure of the hot component is so small. We take the integrated line emissivity to be $\Lambda \approx 5 \times 10^{-23}$ ergs s^{-1} cm^3 for a plasma of several million K (Benjamin et al. 2001). The characteristic cooling time thus derived,

$$t_{cool} = \frac{3kT}{2n\Lambda} \approx 1 \text{ to } 2 \times 10^5 \quad (\text{s}),$$

is many times longer than the characteristic flow time,

$$t_{flow} \equiv \frac{r}{v} \approx \frac{R_*}{v} \approx 2 \times 10^4 \quad (\text{s}).$$

Thus, material shock heated to several million degrees at half a stellar radius above the surface will essentially never cool back down to the ambient wind temperature by radiative cooling, motivating the picture we have presented of a wind with an inner, cool acceleration zone and a quasi-steady-state outer region that is hot, ionized, X-ray emitting, and moving at a more-or-less constant velocity (because it is too highly ionized to be effectively radiatively driven).

Although the scenario we have outlined above is phenomenologically plausible, there are several significant problems with it. First of all, the behavior of wind shocks produced by the line-driven instability is not generally as we have described here. Such shocks tend to propagate outward at an appreciable fraction of the ambient wind velocity (Owocki et al. 1988; Feldmeier et al. 1997). Whereas the scenario we have outlined involves a strong shock that is nearly stationary in the frame of the star, as one would get from running the wind flow into a wall. There is, however, no wall for the wind to run into. It is conceivable that a given shock front forms near $r = 1.5$ R_* and propagates outward, with another shock forming behind it (upstream) at roughly the same radius, so that the ensemble of shocks is close to steady state. However, the narrow observed X-ray lines severely limit the velocity of the shock front, as the post-shock velocity in the star's frame must be greater the shock front's velocity. Yet the observed lines are consistent with a post-shock flow of only $v = 280$ km s^{-1}. A related, second, problem with the scenario is that the shocks required to heat the plasma to $T \approx 2.5$ to 6.5×10^6 K are relatively strong for a weak wind. Smaller velocity dispersions are seen in statistical analyses of the LDI-induced structure in O star winds (Owocki & Runacres 2002). Perhaps the purported wind shocks could be seeded by pulsations at the base of the wind. Seeding the instability at the base has been shown to lead to stronger shocks and more x-ray emission (Feldmeier et al. 1997), though the shocks still propagate relatively rapidly away from the star.

Another problem with this scenario is the very large X-ray production efficiency that is implied. Again, this general problem – that early B stars produce a lot of X-rays given their weak winds – has been known for quite some time. Quantifying it here, using the outer wind shock scenario presented above, and the mass-loss rate of $\dot{M} \approx 10^{-9}$ $M_\odot$ yr^{-1} implied by this analysis, an appreciable fraction of the wind material is heated to X-ray emitting temperatures at any given time. And since the wind must be nearly completely decelerated when it passes through the shock front, a similar fraction of the available wind kinetic energy would go into heating the wind to $T \gtrsim 10^6$ K. The self-excited LDI typically is much less efficient than this (Feldmeier et al. 1997).

If this scenario of a nearly completely shocked-heated outer wind with a low velocity is not likely, then what are the alternatives? As already stated, a more standard model of embedded wind shocks formed by the LDI and outflowing

Any clumping, or deviation from smoothness, in the post-shock region will lead to more emission measure for a given mass-loss rate (and assumed R_0 and v_{100}). Ignoring this effect will lead us to overestimate the mass-loss rate. Thus the mass-loss rate we calculate here of $\dot{M} \approx 10^{-9}$ $M_\odot$ yr^{-1} should be taken to be a crude estimate, subject to a fair amount of uncertainty. However, the two major oversimplifications in this calculation will tend to cancel each other out, as we have just described. We thus conclude that a mass-loss rate of order 10^{-9} $M_\odot$ yr^{-1} is sufficient to explain the observed X-ray emission, assuming a constant, slow outflow of the post-shock plasma above an onset radius of about 1.5 R_*. This mass-loss rate is lower than the predictions of CAK theory but significantly larger than the observed mass loss in the C IV UV resonance line, implying that the actual mass-loss rate of β Cru is in fact lower than CAK theory predicts, but that some of the weakness of the observed UV wind lines is due to ionization effects. Of course, the presence of a large X-ray emitting volume in the outer wind provides a ready source of ionizing photons that can easily penetrate back into the inner, cool wind and boost the ionization state of metals in the wind. In the case of carbon, C V must be the dominant stage of carbon, at least at locations close to the onset radius of shock heating and X-ray emission.

with the wind cannot explain the very modest X-ray emission line widths nor the relatively large emission measures (or shock heating efficiency). However, a standard coronal-type scenario, as applied successfully to cool stars, cannot explain the data either. Coronal sources do not have emission lines that can be resolved in the *Chandra* HETGS. And the f/i ratios would be lower than observed if the hot plasma were magnetically confined near the surface of the star. And of course, there is no reasonable expectation of a strong dynamo in OB stars. The lack of variability would also seem to argue against an origin for the X-rays in a traditional corona at the base of the wind.

Perhaps magnetic fields are involved, but just not in the context of a dynamo and corona. Magnetic channeling of hot-star winds has been shown to efficiently produce X-rays and that X-ray emission has only modestly broad emission lines (Gagné et al. 2005). There is, however, no indication that β Cru has a magnetic field. However, a field of only $B \approx 5$ G would be sufficiently strong to channel the low-density wind of β Cru. The degree of magnetic confinement and channeling can be described by the parameter

$$\eta_* \equiv \frac{B^2 \mathrm{R}_*^2}{\dot{M} v_\infty},$$

where values of $\eta_* > 1$ imply strong magnetic confinement and B is the equatorial field strength for an assumed dipole field (ud-Doula & Owocki 2002). We note that a stronger field has already been detected in another β Cephei star, β Cep itself (Donati et al. 2002), though attempts to detect a field on β Cru have not yet been successful (Hubrig et al. 2006). The upper limits on the field strength are roughly an order of magnitude higher than what would be needed for significant confinement and channeling, though. We also note that the radius of the last closed loop scales as $\eta_*^{0.5}$ (ud-Doula & Owocki 2002), so a field of 50 G – still undetectable – would lead to a magnetosphere with closed field lines out to 3 R_*, consistent with the value found for R_{fir}in §4.1.3.

In a more speculative scenario, It is possible that the material giving rise to the X-ray emission is near the base of the wind, and is falling back toward the star – a failed wind. A similar scenario has been invoked to explain the X-ray emission from τ Sco (B0.2 V) (Howk et al. 2000), which subsequently had a complex surface magnetic field detected on it (Donati et al. 2006). If material gets accelerated off the surface by radiation pressure, but after moving a distance off the surface finds that it can no longer be accelerated – perhaps because of the formation of optically thick clumps - those clumps may stall or even fall back toward the star and interact with the ambient wind, leading to shock heating of wind material and material on the surfaces of the clumps. The problems with this scenario include the ad hoc nature of the clump formation and wind fall-back (though this behavior is in fact seen in conjunction with magnetic channeling (ud-Doula & Owocki 2002; Gagné et al. 2005)) and the f/i ratios which indicate that the hot material is several stellar radii above the surface. *Chandra* observations of τ Sco do show f/i ratios consistent with hot plasma significantly above the photosphere and they also show only modestly broadened X-ray emission lines, similar to what we see in β Cru, although the spectrum of τ Sco is significantly harder (Cohen et al. 2003).

Finally, perhaps the physical characteristics of a wind with a slow, hot outer component that we described in our initial scenario is correct – that is what the f/i ratios and the line widths are telling us – but the heating mechanism is not LDI-related wind shocks. Instead a more complete plasma treatment may be required to describe at least the outer wind, where the densities are below 10^8 cm^{-3}. In such low density winds, the radiatively driven ions can decouple from the protons and rapidly accelerate, leading to frictional heating (Springmann & Pauldrach 1992; Gayley & Owocki 1994; Krtička & Kubát 2001; Owocki & Puls 2002). Heating to X-ray emitting temperatures is predicted to occur only at about spectral type B5 (Krtička & Kubát 2001), but perhaps if the wind mass-loss rates of B stars are lower than anticipated significant frictional heating could occur in early B stars, like β Cru.

We point out that the energy requirements for heating the low density ($n < 10^8$ cm^{-3}) outer wind of β Cru are not severe at all. The heating mechanism might even involve wave propagation if there is even a weak magnetic field on this star. And once significantly heated, such low density circumstellar matter will tend to remain hot, due to the inefficiency of radiative cooling (Owocki 2004). In this sense, the hot plasma in the wind of β Cru could be considered a corona, and though likely initiated by radiation pressure as described in CAK theory, the low-density, slow, far wind of β Cru might even be driven by gas pressure gradients not unlike the situation in the solar wind.

None of these scenarios of X-ray production on β Cru are both physically natural and also in agreement with all the available data. Although, if a magnetic field were to be detected on β Cru, then the magnetically channeled wind shock interpretation would be quite reasonable. However, we stress that the main characteristics that constrain any models that may be put forward are quite secure: the plasma temperature is several million degrees; the emission is not highly variable, except for the periodic hard X-ray variability; the X-ray emission lines are broadened but only modestly so; and the X-ray production efficiency (if the X-ray emission is related to the star's wind) is rather high. Finally, we note that the periodic signal in the hard X-rays and its phasing with the radial velocity variability might be a clue to the X-ray production mechanism.

Put in the context of the empirical X-ray spectral properties of OB stars, the case of β Cru may be extreme but it seems to lie at one end of a continuum of line-profile behavior in hot stars with radiation-driven stellar winds. The late-type O stars δ Ori (Miller et al. 2002) and σ Ori A (Skinner et al. 2004) have lines that are broad, but not as broad as would be expected in the standard wind-shock scenario given their known wind properties. Perhaps there is a gradual transition from stars with X-ray emission lines consistent with their fast stellar winds, such as ζ Pup (Kahn et al. 2001; Cassinelli et al. 2001; Kramer et al. 2003) and ζ Ori (Cohen et al. 2006), through some late O stars with X-ray lines of intermediate width, to early B stars like β Cru for which *Chandra* can barely resolve their lines.

The newly discovered companion to β Cru is most likely a low-mass pre-main-sequence star, similar to the post T Tauri stars found in the *ROSAT* data (Park & Finley 1996; Alcalá et al. 2002). It has a hard, thermal spectrum as PMS stars do, and shows significant variability, again, as PMS stars do. The age of β Cru is less than the pre-main-sequence

lifetimes of most low-mass stars. Lindroos (1986) identified a few dozen B stars with likely PMS companions. If this newly discovered companion indeed is a PMS star, then β Cru would be a Lindroos binary. As such, it would be useful for testing evolutionary models if an optical spectrum of the companion can be obtained. It would be especially helpful if enough information about the mid-B spectroscopic companion (which is supposed to still be on the main sequence (Aerts et al. 1998)) can also be obtained.

Given the companion's X-ray luminosity of nearly 10^{30} ergs s^{-1} cm^{-2} at the assumed distance of 108 pc, even a G star somewhat above the main sequence would have a f_X/f_V ratio consistent with those seen in PMS stars. A somewhat later spectral type is more likely, of course. The nearby K and M post-T Tauri stars detected in the *ROSAT* pointing are typically $13^{\rm th}$ magnitude and have $f_X/f_V \approx 10^{-2}$ (Park & Finley 1996). If the companion has a similar X-ray-to-V-magnitude flux ratio, then it is a 12th magnitude PMS K star. If the magnitude difference between β Cru and this newly discovered companion is roughly 11, then at a separation of $4''$ and with the primary being so bright, detecting it with a ground-based optical or IR telescope will be a challenge; though such data would obviously be very useful for confirming its PMS status and characterizing its properties. Any accretion disk it might have would be significantly irradiated by UV light from the primary. Finally, given a projected separation of 430 AU, the companion should have an orbital period (around β Cru and its spectroscopic companion) of at least 1000 years.

ACKNOWLEDGMENTS

Support for this work was provided by the National Aeronautics and Space Administration through Chandra Award Numbers GO2-3030A and AR7-8002X to Swarthmore College, issued by the Chandra X-ray Observatory Center, which is operated by the Smithsonian Astrophysical Observatory for and on behalf of the National Aeronautics and Space Administration under contract NAS8-03060. MAK was supported by a Eugene M. Lang Summer Research Fellowship from the Provost's Office at Swarthmore College. The authors thank Stan Owocki and Ken Gayley for fruitful discussions, especially about the physics of low density winds and the role of pulsations, and Maurice Leutenegger for sharing his insights about analyzing grating spectra and for the use of his XSPEC models which we employed for modeling the He-like f/i ratios and the wind-broadened lines. We thank Conny Aerts and Jan Cuypers for very helpful discussions about β Cephei variables and for sharing unpublished data with us. We also thank Mark Janoff for some preliminary work on the data analysis. This research has made use of the SIMBAD database, operated at CDS, Strasbourg, France. This research has made use of NASA's Astrophysics Data System Bibliographic Services.

REFERENCES

Abbott D.C., 1982, ApJ, 259, 282
Aerts C., De Cat P., Cuypers J., Becker S.R., Mathias P., De Mey K., Gillet D., Waelkens C., 1998, A&A, 329, 137
Alcalá J.M., Covino E., Melo C., Sterzik M.F., 2002, A&A, 384, 521
Benjamin R.A., Benson B.A., Cox D.P., 2001, ApJ, 554, L225
Blumenthal G.R., Drake G.W.F., Tucker W.H., 1972, ApJ, 172, 205
Bouret J.-C., Lanz T., Hillier D.J., 2005, A&A, 438, 301
Cash W., 1979, ApJ, 228, 939
Cassinelli J.P., Miller N.A., Waldron W.L., MacFarlane J.J., Cohen D.H., 2001, ApJ, 554, L55
Castor J.I., Abbott D.C., Klein R.I., 1975, ApJ, 195, 157
Cohen D.H., Cooper R.G., MacFarlane J.J, Owocki S.P., Cassinelli J.P., Wang P., 1996, ApJ, 460, 506
Cohen D.H., Cassinelli J.P., & MacFarlane J.J, 1997, ApJ, 487, 867
Cohen D.H., Leutenegger M.A., Grizzard K.T., Reed C.L., Kramer R.H., Owocki S.P., 2006, MNRAS, 368, 1905
Cohen D.H., Leutenegger M.A., Townsend R.H.D., 2007, in *Clumping in Hot Star Winds*, Potsdam: Univ.–Verl., eds. W.-R. Hamann, A. Feldmeier, & L. Oskinova, in press
Cohen D.H., de Messières G.E., MacFarlane J.J., Miller N.A., Cassinelli J.P., Owocki S.P., Liedahl D.A., 2003, ApJ, 586, 495
Cuypers J., 1983, A&A, 127, 186
Cuypers J., Aerts C., Buzasi D., Catanzarite J., Conrow T., Laher R., 2002, A&A, 392, 599
Davis J.E., 2001, ApJ, 562, 575
Donati J.-F., Wade G.A., Babel J., Henrichs H.F., de Jong J.A., Harries T.J., 2002, MNRAS, 326, 1265
Donati J.-F., et al., 2006, MNRAS, 370, 629
Drew J.E., Denby M., Hoare M.G., 1994, MNRAS, 266, 917
Favata R., Flaccomio E., Reale F., Micela G., Sciortino S., Shang H., Stassun K.G., Feigelson E.D., 2005, ApJ, 160, 469
Feigelson E.D, Lawson W.A., 1997, AJ, 113, 2130
Feldmeier A., Puls J., Pauldrach A.W.A., 1997, A&A, 322, 878
Fruscione A., Hawkins I., Jelinsky P., Wiercigroch A., 1994, ApJ, 94, 127
Fullerton A.W., Massa D.L., Prinja R.K., 2006, ApJ, 637, 1025
Gagné M., Oksala M., Cohen D.H., Tonnesen S.K., ud-Doula A., Owocki S.P., Townsend R.H.D., MacFarlane J.J., 2005, ApJ, 628, 986
Gayley K.G., Owocki S.P., 1994, ApJ, 434, 684
de Geus E.J., de Zeeuw P.T., Lub J., 1989, A&A, 216, 44
Hanbury Brown R., Davis J., Allen L.R., 1974, MNRAS, 167, 121
Heintz W., 1957, The Observatory, 77, 200
Hillier D.J., Kudritzki R.–P., Pauldrach A.W.A., Baade D., Cassinelli J.P., Puls J., Schmitt J.H.M.M., 1993, ApJ, 276, 117
Hiltner W.A., Garrison R.F., Schild R.E., 1969, ApJ, 157, 313
Howk J.C., Cassinelli J.P., Bjorkman J.E., Lamers H.J.G.L.M., 2000, ApJ, 534, 348
Hubrig S., Briquet M., Schöller M., De Cat P., Mathys G., Aerts C., 2006, MNRAS, 369, L61
Kahn S.M., Leutenegger M.A., Cottam J., Rauw G., Vreux J.–M., den Boggende A.J.F., Mewe R., Güdel M., 2001, A&A, 365, L312

Kastner J.H., Huenemoerder D.P., Schulz N.S., Canizares C.R., Weintraub D.A., 2002, ApJ, 567, 434
Kramer R.H., Cohen D.H., Owocki S.P., 2003, ApJ, 592, 532
Krtička J., Kubát J., 2001, A&A, 359, 983
Kudritzki R.P., Pauldrach A.W.A., Puls J., Abbott D.C., 1989, A&A, 219, 205
Lanz T., Hubeny I., 2007, ApJ, 169, 83
Leutenegger M.A., Paerels F.B.S., Kahn S.M., Cohen D.H., 2006, ApJ, 650, 1096
Liedahl D.A., Kahn S.M., Osterheld A.L., Goldstein W.H., 1990, ApJ, 350, L37
Lindroos K.P., 1985, A&AS, 60, 183
Lindroos K.P., 1986, A&A, 156, 223
Marshall H.L., Dewey D., Ishibashi K., 2004, SPIE, 5165, 457
Mathias P., Gillet D., Crowe R., 1992, A&A, 257, 681
Miller N.A., Cassinelli J.P., Waldron W.L., MacFarlane J.J., Cohen D.H., 2002, ApJ, 577, 951
Morrison R., McCammon D., 1983, ApJ, 270, 119
Niemczura E., Daszynska-Daszkiewicz J., 2005, A&A, 433, 659
Owocki S.P., 2004, *Evolution of Massive Stars, Mass Loss and Winds*, EAS Publication Series, eds. M. Heydari-Malayeri, Ph. Stee, J.-P. Zahn, 13, 163
Owocki S.P., Castor J.I., Rybicki G.B., 1988, ApJ, 335, 914
Owocki S.P., Cohen D.H., 2001, ApJ, 559, 1108
Owocki S.P., Cranmer S.R., 2002, *I.A.U. Coll. 185*, ASP: San Francisco, eds. C. Aerts, T. R. Bedding, J. Christensen-Dalsgaard, 259, 512
Owocki S.P., Puls J., 2002, ApJ, 568, 965
Owocki S.P., Runacres M.C., 2002, A&A, 381, 1015
Paltani S., 2004, A&A, 420, 789
Park S., Finley J.P., 1996, AJ, 112, 693
Perryman M.A.C., et al., 1997, A&A, 323, L49
Popper D.M., 1968, ApJ, 151, L51
Porquet D.,Dubau J., 2000, A&AS, 143, 495
Prinja R.K., 1989, MNRAS, 241, 721
Schmitt J.H.M.M., Robrade J., Ness J.-U., Favata F., Stelzer B., 2005, A&A, 432, L35
Smith R.K, Brickhouse N.S., Liedahl D.A., Raymond J.C., 2001, ApJ, 556, L91
Skinner S., Cohen D.H., Gagné M., Owocki S.P., Townsend R.H.D., 2004, BAAS, 20510517S
Stankov A., Handler G., 2005, ApJ, 158, 193
Springmann U.W.E., Pauldrach A.W.A., 1992, A&A, 262, 515
ud-Doula A., Owocki S.P., 2002, ApJ, 576, 413
Uesugi A., Fukuda I., 1982, *Catalogue of stellar rotational velocities (revised)*, Kyoto: University of Kyoto, Department of Astronomy
Worley C.E., Douglass G.G., 1997, A&AS, 125, 523
Zhekov S. A., Palla F., 2007, MNRAS, in press (arXiv:0708.0085)